ASTFE American Society of Thermal and Fluids Engineers

10th Thermal and Fluids Engineering Conference (TFEC)
March 9-12, 2025
Partially Online Virtual and at George Washington University, DC Conference

TFEC-2025-56033

Transmission interference fringe (TIF) for evaporating droplet's contact angle variation

Iltai Isaac Kim[1*], Yang Lie[1,2], Jeffery A. Greathouse[3], and Hongkyu Yoonr[3]

[1]1Texas A&M University-Corpus Christi, 6300 Ocean Dr. Corpus Christi, TX 78412-5797, USA
[2]Pro-Lab Diagnostics, 21 Cypress Blvd, Round Rock, TX 78665, USA
[3]Sandia National Laboratories, Albuquerque, NM, 87185, USA

ABSTRACT

The transmission interference fringe (TIF) technique is developed to determine the contact angle successfully by geometric formulation. The TIF's characteristics are explored using the incidence angle and the refractive index of liquids. The TIF is employed to measure the contact angle variation of the evaporating droplets in experiments, observing the contact angle increases with the transmission interference fringe formation close to dry-out. This finding is against the general observation of constantly decreasing contact angle during constant contact radius evaporation. The interference fringe formation is caused by the convex-concave profile, not a pure convex, indicating nonuniform evaporative flux along the droplet surface. TIF offers enhanced visualization capabilities and expanded measurement ranges compared with the existing techniques. The technique represents a valuable tool in the study of droplet dynamics, offering insights into phenomena that were previously challenging to observe and measure.

KEY WORDS: Transmission, Interference fringe, Evaporation, Contact Angle, Refractive Index, Constant Contact Radius, Reflection

1. INTRODUCTION

The contact angle (*CA*) is a key determinant of the material's surface energy in the classical Young's equation [1]. It plays a pivotal role in a myriad of wetting behaviors in liquid-solid-vapor interactions, binding, coating, evaporation, condensation, and superrepellency. Its applications span across various fields such as micro/nanofluidics, ionic liquids separator and membrane, oil recovery, printing, and more. Most physical and chemical phenomena in natural and synthetic systems involve the CA and corresponding surface energy interaction, underscoring the importance of CA. A microscope setup has been widely used to measure CAs in multiple applications. However, there are many limitations in the microscopic measurement of CA. Campbell et al. [2] showed low CA measurement using the lens effect, Cha et al. [3] measured various CAs using focal plan imaging, Frankel et al. [4] observed the droplet profile using total internal fluorescence. Sundberg et al. [5] measured CA using interference, all based on a microscopy setup. These techniques are effective only for small (diameter less than 1 mm) droplets [6]. Side-view imaging using a goniometer and the top imaging technique [7] can detect CAs with various droplet sizes, but these techniques have difficulty in measuring small CAs. Recently, aperture total internal reflection (A-TIR) was employed to measure a broad range of CAs (0~90°) in a simple setup without the need of a microscope configuration, but has a limitation for real-time analysis since the measurement requires the usage of two different apertures sequentially [8]. This highlights the need for a more versatile and precise method such as the transmission interference fringe (TIF) technique. The refractive index of liquids is measured by the critical angle method [9, 10], interferometric techniques [11], and surface plasmon resonance (SPR) [10]. Allain et al. [12] and Guo et al. [13] measured the CA using the normal transmission and the oblique reflection, respectively. However, it has yet to be studied systematically since.

*Corresponding Author: ikim@tamucc.edu

In this research, the *TIF* technique at oblique angles is introduced to determine the CAs of liquid droplets. Recently, the reflection interference fringe technique was introduced by the authors [14, 15], and we want to expand its application to the transmission mode and apply it to real-time *CA* detection during the evaporation process. Its working principle is explained by geometric formulation, and the characteristics are explored by experiments and simulations with the parameters of the incidence angle relevant to the rail angle and the refractive index of the droplet liquids. Furthermore, the *TIF* is successfully applied to the evaporating droplet's *CA* variation where the constant contact radius (*CCR*) evaporation shows an increasing *CA* at the end of dry-out and forms a convex-concave droplet profile, which is reported for the first time to the best of authors' knowledge. The finding of increasing CA is against the general observation that the CA decreases during the CCR evaporation. Furthermore, the observation of the convex-concave profile from the formation of the transmission interference fringe shows the evaporative flux is not uniform along the droplet radius, which corresponds to the existing report [16].

2. TRANSMISSION INTERFERENCE FRINGE (*TIF*) TECHNIQUE

The *TIF* is formed when a droplet is placed on a flat substrate in a transmission optical system and illuminated by a He-Ne laser (λ = 633 nm). Fig. 1-a shows the installed experimental schematic. A coherent and magnified laser beam with a diameter of 5 cm is incident on the sample and transmitted to form a magnified fringe on the screen away from the sample at a working distance of 300 mm. The transmitted beam is projected on a screen in the shape of a magnified beam through a droplet lens effect. The employed droplets would be macro sizes with diameters of 1~10 mm and heights of 20~2000 μm. The non-evaporating droplets can be assumed to have spherical profiles [8, 9]. The fringe radius (FR) is measured from the laser center to the edge of the fringe on the far-field screen (Fig. 1-b). It is observed that the fringe radius (*FR*) is proportional to the *CAs* of the droplets. Thus, the geometric relation is analyzed as in Fig. 2 to show that the *FR* is directly proportional to the droplet' CA.

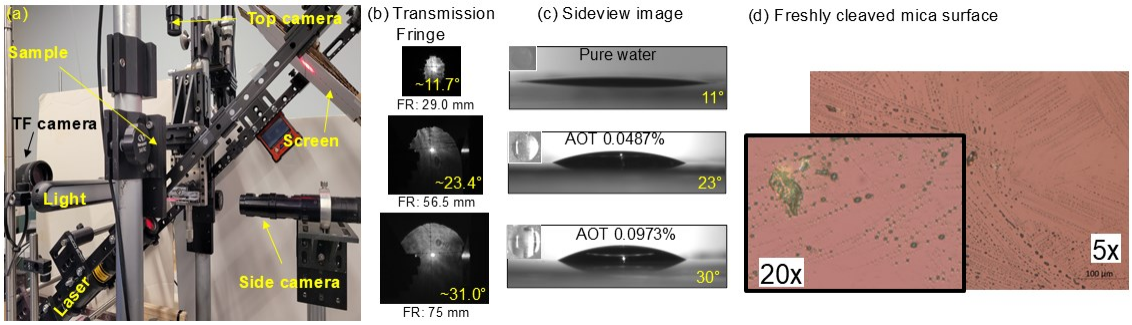

Fig. 1 The experimental setup of the *TIF* technique and *TIF* images.

Fig 1-b shows the *TIF* images for the hexadecane oil droplet on the flat surface of freshly cleaved mica with different surfactant (AOT) concentrations. Fig. 1-c is the side-view images corresponding to the *TIF* images. Fig. 1-b and c show that the *TIF* is an effective measurement technique for *CA* to investigate the effect of anionic surfactant AOT on the *CA* of hexadecane oil on the cleaved mica surfaces. The cleaved mica surface is believed to have the perfectly clean surface [17]. Fig. 1-d is an optical microscope image for the freshly cleaved mica surface. The figure shows that the CA increases with AOT concentration [17, 18]. The *CA* is calculated by the following geometric formulation (Eq. (5)), which will be discussed below. The *CAs* were compared between the *TIF* technique and the side-view imaging to show excellent agreement, indicating that *TIF* is an effective measurement technique for *CA*. The *CA* is estimated to increase because the hydrophobic tail of the AOT molecules concentrates at the liquid-vapor interface, resulting in a higher *CA* at higher AOT concentrations [17]. In most droplets, the contact line is located at the droplet edge. The apparent *CA* is determined at the edge with the maximum slope. The outermost fringe is caused by the reflection where the CA is measured. The refracted length inside the droplet (less than 10 mm) is much smaller than the current working distance (*WD*) of 100 ~ 300 mm, and the *WD* is assumed to be straight from the droplet center to the far-field screen.

The analytic relation between the *FR* and the *CA* can be obtained from the following geometric formulation at the oblique incidence angle in Fig. 2. The coordinates for the screen center (x_c, y_c) and the location of the outermost fringe (x_{FR}, y_{FR}) are determined by the trigonometry.

$$(x_c, y_c) = (WD\cos\theta_{Rail}, WD\sin\theta_{Rail}),\ (x_{Fr}, y_{Fr}) = (x_c - FR\sin\theta_{Rail}, y_c - FR\cos\theta_{Rail}) \quad (1)$$

where θ_{RAIL} is the rail angle of the transmission optical axis. The linear line for the edge ray refracted at the droplet edge with the droplet radius of a is

$$y = k_1(x - a), k_1 = tan(90° - (\theta_{Trn34} + \theta_C)) \quad (2)$$

where and k_1 is the parameter incorporating the RI of liquids, θ_{Trn34} is a function of the droplet CA (θ_c) as shown in the relations in Fig. 2. The linear line for the screen is

$$y = k_2(x - x_c) + y_c, k_2 = -\frac{1}{tan\,\theta_{Rail}} \quad (3)$$

By equaling Eqs. (2) and (3) at (x_{FR}, y_{FR}),

$$k_1(x_{Fr} - a) = k_2(x_{Fr} - x_c) + y_c \;,\; x_{Fr} = \frac{k_1 a - k_2 x_c + y_c}{k_1 - k_2} = x_c - FR \sin\theta_{Rail} \quad (4)$$

Thus, the *FR* is analytically obtained as follows:

$$FR = \frac{k_1(x_c - a) - y_c}{(k_1 - k_2)\sin\theta_{Rail}} = \frac{k_1(WD\cos\theta_{Rail} - a) - WD\sin\theta_{Rail}}{k_1\sin\theta_{Rail} + cos\theta_{Rail}} \quad (5)$$

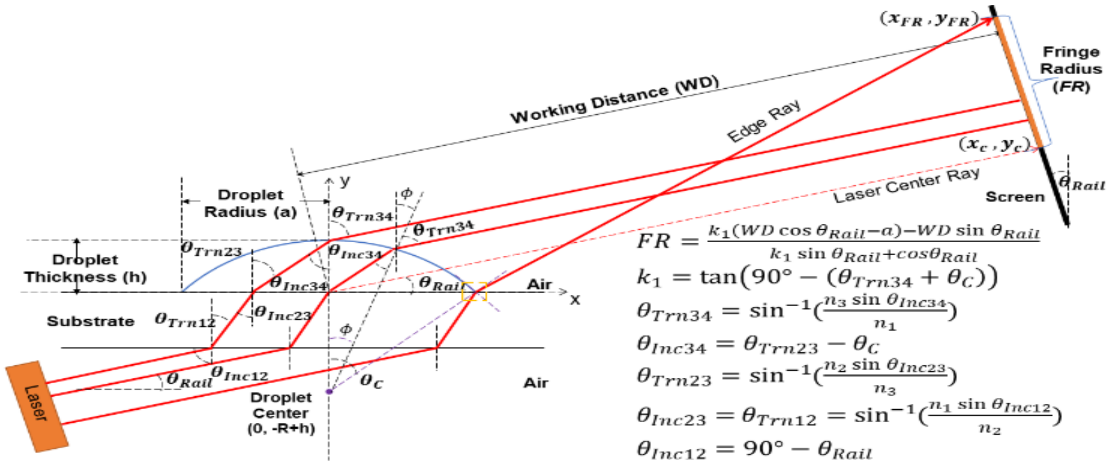

Fig. 2 The schematic of *TIF* technique and the geometric formulation.

3. CHARACTERISTICS OF TRANSMISSION FRINGE

A. Incidence angle (Rail angle)

Fig. 3-a shows the *CA* versus the *FR* and the laser incidence angles (θ_{inc}=θ_{inc23}) with the hexadecane oil (*RI* 1.434 at 633 nm wavelength), which is obtained from the geometric formulation (Eq. (5)). The incidence angle is inversely proportional to the rail angle as in Fig. 2. The simulation from the geometric formulation is shown as lines with five different rail angles for the rail angles of 10, 30, 40, 50, and 90°, respectively. The experiment is shown as symbols for the rail angles of 30, 40, and 50°, respectively. It shows a saturation trend to reach a certain level of *CA* above some *FR*. Fig. 3-b is a zoomed-in view of Fig. 3-a for the smaller *CAs* less than 30 degrees. The *CA* increases with an increasing *FR* at a fixed incidence angle. It also shows that the *FR* increases with a decreasing rail angle, corresponding to the increasing incidence angle, at the same *CA*; for example, at the *CA* of 10°, the *FR*s are from 9, 11, 15, 19, and 40 mm for 90, 50, 40, 30, and 10 rail angles. Fig. 3-c shows the zoom-in view for contact angles less than 5 degrees. The simulation shows that the small rail angles can determine an extensive contact angle range of up to 90° and determine lower *CA* of less than 1°. In comparison, the higher rail angles such as normal incidence (90°) cannot measure less than 2° and more than 45°. This is why the oblique *TIF* method needs to be employed compared to the normal incidence fringe method.

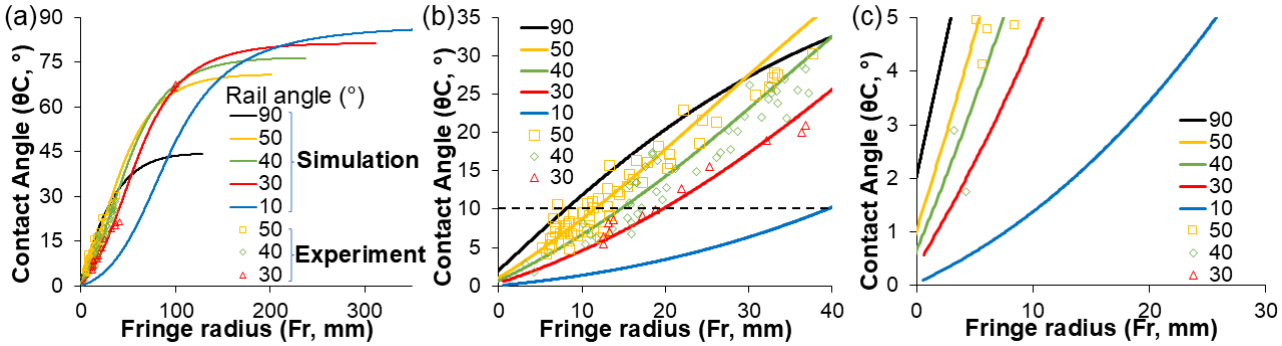

Fig. 3 The determination of the *CA* by the measured *FR*.

B. Refractive index (*RI*)

Based on the functional relationship (Eq. (5)) between the *CA* and the *FR*, the effect of the *RI* of liquids on the *CAs* is explored with the measured *FR*. Fig. 4 shows the *CA* dependency on the *RI* and the *FR* by simulation and experiment. The figure shows the refractive index contour with color variation with five representative different refractive indexes: *RI*=1.3, 1.4, 1.5, 1.6, and 1.73. The *RI* liquids from Cargille Lab are used. The experiment shows a good agreement with the simulation. It shows that the *CA* decreases with increasing *RI* of liquids at the same *FR*. The figure also shows the increasing *CA* with the *FR* as in Fig. 3. Fig. 4 is an exciting result as the *TIF* technique can determine the RI of unknown liquids if we can measure the *FR* and the *CA*. In RI determination, the *CA* can be measured by the side-view imaging.

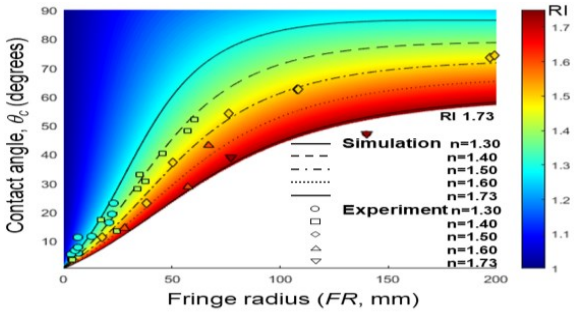

Fig. 4 The *CA* dependency on the refractive index of liquids. θ_{RAIL}=40°and *WD*=130 mm.

The uncertainty analysis is conducted concerning the *CA* (θ_c), which is Eq. S20 in a recent publication [19] and is obtained from Eq. (5), as a function of the droplet radius, the working distance, the droplet refractive index, the rail angle, and the *FR* with elementary uncertainty of 5 % [20], providing the normalized uncertainty of ~ 5 %, which shows a good measurement confidence.

4. EVAPORATING DROPLET'S CONTACT ANGLE CHANGE

The *TIF* technique is employed to monitor the *CA* variation by the fringe radius during the water droplet's evaporation. One micro-liter (µl) water droplet is placed on the cleaned glass substrate at room temperature and ambient conditions. Fig. 5 shows the time-elapsed *TIF* images of the evaporating droplet until full dry-out with the corresponding side-view and top-view images. The top-view images are in the middle row. In *TIF* images, the measured fringe radii are at the top-right corner, and their corresponding *CAs* are at the bottom. The *FR* is from the brightest spot center to the edge of the *TIF* upward. The upper fringe corresponds to the right side of the droplet, as in Fig. 2. The droplet radius (*a*) is 1.26 mm. In the side-view images at the bottom row of the figure, the measured *CA* and the height are on the images' bottom. The evaporation is in the constant contact radius (*CCR*) mode, as the droplet contact line doesn't change during evaporation, as seen from the top-view. The droplet initially follows the spherical profile with almost the same height of 350 µm from the side-view imaging and the analytical relation ($CA = tan^{-1}(2ah/(a^2-h^2))$). With time, water liquid evaporates to vapor at the same contact line; thus the initial spherical profile turns to the oblate spheroid shape [21].

One unexpected phenomenon was observed at the elapsed time of 520 sec close to the full dry-out, as the *FR* increased from 8mm at 480 sec to 12 mm at 520 sec with the interference fringe formation on the far-field screen. Fig. 6 shows clear distinction between two times. In side-view and top-view imaging, no distinct features were observed, as shown in the images at the time of 540 sec. All images are at the same

scale in each row. The bright spot in the *TIF* images is caused by the transmitted laser. Note that the *TIF* images up to the time of 480 sec observe no interference fringes, although its *FR* gets small.

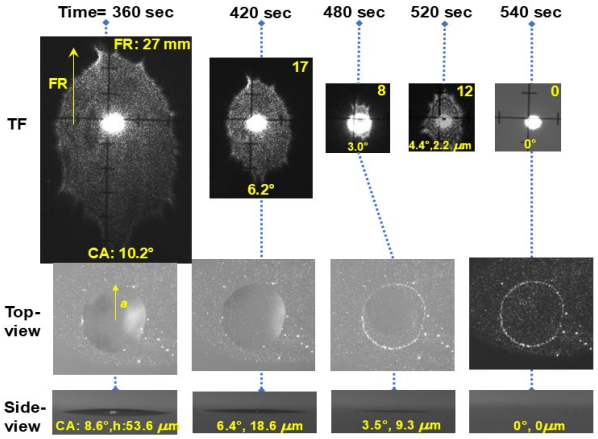

Fig. 5 Time series of evaporating droplet's images (Permission obtained from Applied Physics Letters[19]).

Fig. 6 shows the trend of *CA* and the droplet height for Fig. 5 from the *TIF* and the side-view measurements with zoom-in views of the *TIF* images at 480, 520, and 540 sec. The droplet height is from the side-view measurement. Only the *TIF* image at 520 sec shows the interference fringe formation, much different from the images taken earlier without any fringes, even with an increasing *FR* than the one at 480 sec. The height at 520 sec in the *TIF* image is calculated as 2.2 μm from the optical path difference (Δ) between the apex of the center convex profile and the valley of the contact line concave profile ($\Delta = n_d\,(h-t)/\cos\theta_{trn} = (FN+0.5)\lambda$), a similar form in the recently reported result in the reflection interference fringe [14], where n_d is the refractive index of the droplet liquid (water, 1.3323), h is the droplet height, t is the precursor film thickness (t ~ 100 nm)[22], θ_{trn} is the transmission angle at the interface between the substrate and the droplet ($\theta_{trn} = sin^{-1}(n_s/n_d\ sin\theta_{inc})$, n_s is the refractive index of the substrate (n_s = 1.515), θ_{inc} is the incidence angle, *FN* is the fringe number (*FN*=~5), and λ is the wavelength (λ=633 nm). The fringe radius is directly proportional to the *CA*. Hence, the increasing *FR* means the increasing *CA*, which contrasts with the general observation of decreasing *CA* during the evaporating droplet [21, 23]**.** Furthermore, according to a recent study [14,15], the formation of the interference fringe on the far-field screen is caused by the dual convex-concave profile between the reflection at the convex center apex and the reflection at the concave contact line region. The side-view and top-view imaging could not detect the *CA* increase and the non-convex profile formation during evaporation as the thickness is so tiny, less than ~2 μm. Even a microscope, if located on the bottom, cannot detect a non-convex profile as the interference fringe caused by the dual convex-concave profile of the droplet is formed on a far-field screen, much away from the sample, not on the interface between the droplet and the substrate [14]. Hence, the observation of the non-convex profile during evaporation indicates that evaporative flux along the droplet liquid-air interface is not uniform or the adhesion force between the liquid and substrate varies along the radial direction depending on the liquid film thickness. The nonuniform evaporative flux corresponds to the reported result [16].

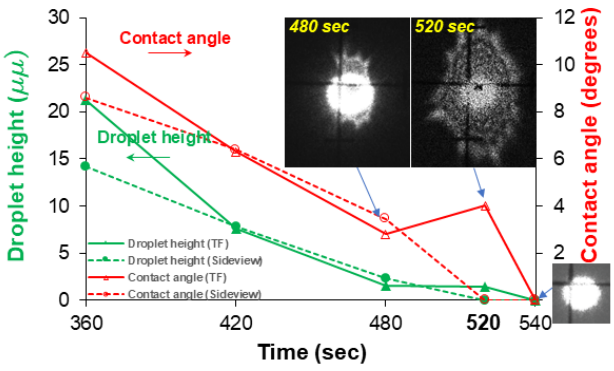

Fig. 6 The CA and the droplet height variation of evaporating droplet.

5. SUMMARY

In this research, we showed that the *TIF* technique can effectively determine the liquid contact angle (*CA*) by measuring the fringe radius (*FR*) formed on a far-field screen away from the droplet in a simple setup. Experiment and geometric simulation show an excellent agreement. The *TIF* characteristics are explored using the droplet's incidence angle and the refractive index. The *TIF* at a higher incidence angle can determine a wide range of contact angles (0~90°) and is especially effective at a lower contact angle of less than 1°, which is not possible with a normal incidence angle. The *TIF* is employed for the contact angle variation of the evaporating droplet to show a contact angle increase by the increasing fringe radius at the end of dry-out in the constant contact radius (*CCR*) mode, which is different from the general observation that the contact angle keeps decreasing during evaporation. Furthermore, the interference fringe is observed to show that the droplet profile has the shape of a convex-concave, not a pure convex profile, showing the nonuniform evaporative flux along the droplet. Hence, the *TIF* can be very effective to determine the contact angle, especially low contact angle of less than 5°, thin liquid film thickness in a micron range, and dual droplet profile in real-time. It is expected to provide a breakthrough in thin film dynamics, such as evaporation, condensation, and wetting, when combined with near-field diagnostics of optical microscope or surface plasmon resonance imaging [24].

ACKNOWLEDGMENT

This work is grounded in a recently published article in Applied Physics Letters [19], viewed from a different perspective. This work was supported by a research grant from CEKO Co., LTD, NSF CBET TTP program (2301973), TAMUS-LANL Development Fellowship, and in part by the Laboratory Directed Research and Development Program at Sandia National Laboratories. A Sandia National Laboratories is a multi-mission laboratory managed and operated by National Technology Engineering Solutions of Sandia, LLC (NTESS), a wholly owned subsidiary of Honeywell International Inc., for the U.S. Department of Energy's National Nuclear Security Administration under contract DE-NA0003525. This written work is authored by an employee of NTESS. The employee, not NTESS, owns the right, title and interest in and to the written work and is responsible for its contents. Any subjective views or opinions that might be expressed in the written work do not necessarily represent the views of the U.S. Government. The publisher acknowledges the U.S. Government license to provide public access under the DOE Public Access Plan. The research is patented about the contact angle and the refractive index detection technique as a US Application as of Dec. 26, 2023 by TAMUS [25].

REFERENCES

1. Drelich, J., J. Long, and A. Yeung, *Determining Surface Potential of the Bitumen-Water Interface at Nanoscale Resolution using Atomic Force Microscopy.* The Canadian Journal of Chemical Engineering, 2007. **85**(5): p. 625-634.
2. Campbell, J.M. and H.K. Christenson, *Dynamic Measurement of Low Contact Angles by Optical Microscopy.* ACS Appl Mater Interfaces, 2018. **10**(19): p. 16893-16900.
3. Cha, H., et al., *In Situ Droplet Microgoniometry Using Optical Microscopy.* ACS Nano, 2019. **13**(11): p. 13343-13353.
4. Franken, M.J.Z., C. Poelma, and J. Westerweel, *Nanoscale contact line visualization based on total internal reflection fluorescence microscopy.* Optics Express, 2013. **21**(22): p. 26093-26102.
5. Sundberg, M., A. Månsson, and S. Tågerud, *Contact angle measurements by confocal microscopy for non-destructive microscale surface characterization.* Journal of Colloid and Interface Science, 2007. **313**(2): p. 454-460.
6. Poulard, C., O. Bénichou, and A.M. Cazabat, *Freely Receding Evaporating Droplets.* Langmuir, 2003. **19**(21): p. 8828-8834.
7. Zhang, H., J. Gottberg, and S. Ryu, *Contact angle measurement using a Hele-Shaw cell: A proof-of-concept study.* Results in Engineering, 2021. **11**: p. 100278.

8. Kim, I.I., Y. Lie, and J.S. Park, *Aperture total internal reflection (A-TIR) for contact angle measurement.* Optics Express, 2021. **29**(25): p. 41685-41702.
9. Park, J.S., et al., *Development of aperture total internal reflection (A-TIR) for micro droplets and fingerprint patterns characterization.* Optics Communications, 2019. **453**: p. 124414.
10. Kim, I. and K.D. Kihm, *Measuring near-field nanoparticle concentration profiles by correlating surface plasmon resonance reflectance with effective refractive index of nanofluids.* Optics Letters, 2010. **35**(3): p. 393-395.
11. Sung, Y., et al., *Three-Dimensional Holographic Refractive-Index Measurement of Continuously Flowing Cells in a Microfluidic Channel.* Physical Review Applied, 2014. **1**(1): p. 014002.
12. Allain, C., D. Ausserre, and F. Rondelez, *A new method for contact-angle measurements of sessile drops.* Journal of Colloid and Interface Science, 1985. **107**(1): p. 5-13.
13. Guo, K.H., W.-J. Yang, and T. Uermurat, *Determination of droplet morphology by laser reflection interferometry.* Optics Letters, 1985. **10**(10): p. 467-469.
14. Kim, I.I., et al., *Investigating the origin of the far-field reflection interference fringe (RIF) of microdroplets.* Journal of Applied Physics, 2024. **135**(20).
15. Kim, I.I., et al. *Determining micro droplet profiles using internal reflection interference fringe (RIF) technique*. in *Frontiers in Optics + Laser Science 2023 (FiO, LS)*. 2023. Tacoma, Washington: Optica Publishing Group.
16. Kuk, M., J. Pyeon, and H. Kim, *Vapor distribution changes evaporative flux profiles of a sessile droplet.* Journal of Colloid and Interface Science, 2023. **652**: p. 646-652.
17. Long, D.M., et al., *Molecular Dynamics Simulation and Cryo-Electron Microscopy Investigation of AOT Surfactant Structure at the Hydrated Mica Surface.* Minerals, 2022. **12**(4): p. 479.
18. Kim, I.I., et al., *Transmission interference fringe (TIF) technique for the dynamic visualization of evaporating droplet.* Applied Physics Letters, 2024. **125**(11): p. 114102.
19. Kim, I.I., et al., *Transmission interference fringe (TIF) technique for the dynamic visualization of evaporating droplet.* Applied Physics Letters, 2024. **125**(11).
20. Kim, I.T. and K.D. Kihm, *Label-free visualization of microfluidic mixture concentration fields using a surface plasmon resonance (spr) reflectance imaging.* Experiments in Fluids, 2006. **41**(6): p. 905-916.
21. Popov, Y.O., *Evaporative deposition patterns: Spatial dimensions of the deposit.* Physical Review E, 2005. **71**(3): p. 036313.
22. Popescu, M.N., et al., *Precursor films in wetting phenomena.* Journal of Physics: Condensed Matter, 2012. **24**(24): p. 243102.
23. Rowan, S.M., M.I. Newton, and G. McHale, *Evaporation of Microdroplets and the Wetting of Solid Surfaces.* The Journal of Physical Chemistry, 1995. **99**(35): p. 13268-13271.
24. Kim, I., et al., *Full-field thickness measurement of ultrathin liquid film in receding contact-induced nano-channel using surface plasmon resonance.* Optics Express, 2018. **26**(16): p. 20975-20989.
25. Park, I.I.K.Y.l.J., *Compositions and methods for evaluation of liquid contact angle properties*, U.P. Office, Editor. 2023: USA.